The Tension Activated Carbon–Carbon Bond

Authors: Yunyan Sun[1,2]†, Ilia Kevlishvili[3]†, Tatiana B. Kouznetsova[4], Zach P. Burke[1], Stephen L. Craig[4]*, Heather J. Kulik[3,5]*, and Jeffrey S. Moore[1,2]*

Affiliations:

[1]Department of Chemistry, University of Illinois at Urbana−Champaign, Urbana, Illinois 61801, USA.

[2]Beckman Institute for Advanced Science and Technology, University of Illinois at Urbana−Champaign; Urbana, IL 61801, USA.

[3]Department of Chemical Engineering, Massachusetts Institute of Technology; Cambridge, MA, USA.

[4]Department of Chemistry, Duke University; Durham, NC, USA.

[5]Department of Chemistry, Massachusetts Institute of Technology; Cambridge, MA, USA.

† Those authors contributed equally to this work

*Corresponding authors. Email: stephen.craig@duke.edu (S.L.C); hjkulik@mit.edu (H.J.K); jsmoore@illinois.edu (J.S.M)

Abstract:

Over the last century, chemists have mastered the ability to precisely connect pairs of carbon atoms for the synthesis of complex structures ranging from pharmaceuticals to polymeric materials. Less attention has been given to precision C–C bond disconnection. In the past two decades, mechanical force has emerged as a unique vectoral stimulus to drive selective and productive C–C bond activations[1], leading to distinct reaction trajectories[2,3] as well as unprecedented mechanoresponsive materials[4]. However, the molecular details of force to chemical transduction are poorly captured by conventional chemical intuition, making it challenging to understand and predict structure-reactivity relationships under tension[5,6]. Here, we utilize a physical organic model inspired by the classical Morse potential and its differential forms to identify the effective force constant (k_{eff}) and the force-free reaction energy (ΔE) as key molecular features that govern mechanochemical kinetics. Through a comprehensive experimental and computational investigation with four norborn-2-en-7-one (NEO) mechanophores, we establish the relationship between these features and the force-dependent energetic changes along the reaction pathways. We found a linear model accurately predicts the transition force (f^*) required for C–C bond activation in over 30 mechanophores. These results demonstrate a general mechanistic framework for mechanochemical reactions under tensile force, and provide a highly accessible tool for the large-scale computational screening in the design of mechanophores.

Main:

The carbon–carbon (C–C) bond is widely acknowledged for its strength, yet its scission is surprisingly common in a diverse array of selective mechanochemical transformations[7]. These transformations, which are the defining characteristic of mechanophores, often exploit the homolytic activation of C–C bonds to achieve desired chemical[8,9]and physical changes[10-13]. Despite the number of mechanophores and computational tools for mechanochemical modeling[7,14], examining C–C bond reactivity under tension typically requires extensive experimental efforts or highly involved electronic structure calculations[5,9,11], limiting the discovery of new mechanophores. We, therefore, sought a simple and predictive model of mechanochemical reactivity that connects state-of-the-art *ab initio* computations to concepts from the physical organic canon in a way that is immediately useful, intuitive to non-specialists, and provides a framework for further refinement.

The tension-activated bond hypothesis

The classical Morse potential with its anharmonic shape motivates the concept of an effective force constant and reaction energy for mechanochemical transformations in polyatomic molecules where C-C bond scission is the rate-determining step (RDS). The Morse function describes the potential of diatomic molecules that have an equilibrium bond length of L_0 and bond dissociation energy U_0 (**Fig. 1a**). The derivative of the Morse function with respect to interatomic displacement yields the restoring force curve that describes how strongly the pair of atoms are pulled toward L_0 for a given displacement, ΔL. The slope of the restoring force curve at L_0 is the Hookean force constant, k, which characterizes the bond's stiffness or resistance to deformation. The maximum value of the curve corresponds to f_{max} and the area under the force curve corresponds to U_0. We introduce the restoring force triangle as a helpful mnemonic that approximates the restoring force curve (**Fig. 1a),** characterized by its area ($\sim U_0$), front slope k, and back slope ($-k/8$), derived from the inflection point of the restoring force curve (fig. S1). In contrast to the simple uniaxial loading of force in diatomic molecules, the transfer of forces in polyatomic molecules becomes more intricate due to the influence of stereochemical and electronic features from substituents attached to carbon atoms (i.e., handles), known as the lever-arm effect[5,6,15]. To model force transmission from remote handles (**Figs. 1b** and **1c**), we define the effective force constant (k_{eff}). Additionally, we replace the diatomic term U_0 with the reaction energy ΔE, representing the change in bond energy from the force-free ground state, GS, to the diradical intermediate in polyatomic molecules (**Fig. 1b**).

When a constant tension, f_0, is applied to the handles, the C–C bond stretches until the force is balanced by the molecule's internal restoring force (**Fig.1b**). A new minimum point is generated on the resulting force-modified potential energy surface (FMPES, blue dashed line)[16,17] , which is named the tension-activated bond (TAB) (**Fig. 1c**). The FMPES exhibits an activation barrier at the local maximum, which occurs at a specific bond displacement where the applied force intersects with the downward slope of the restoring force triangle (fig. S2). This position corresponds to the tensioned transition state (TTS) for bond dissociation. Further deformation beyond the TTS leads to the formation of a tensioned diradical intermediate (TI) (**Figs. 1b and 1c**). Notably, when f_0 equals f_{max}, the TAB and TTS converge to a single geometry, enabling the reaction to proceed through a barrierless process.

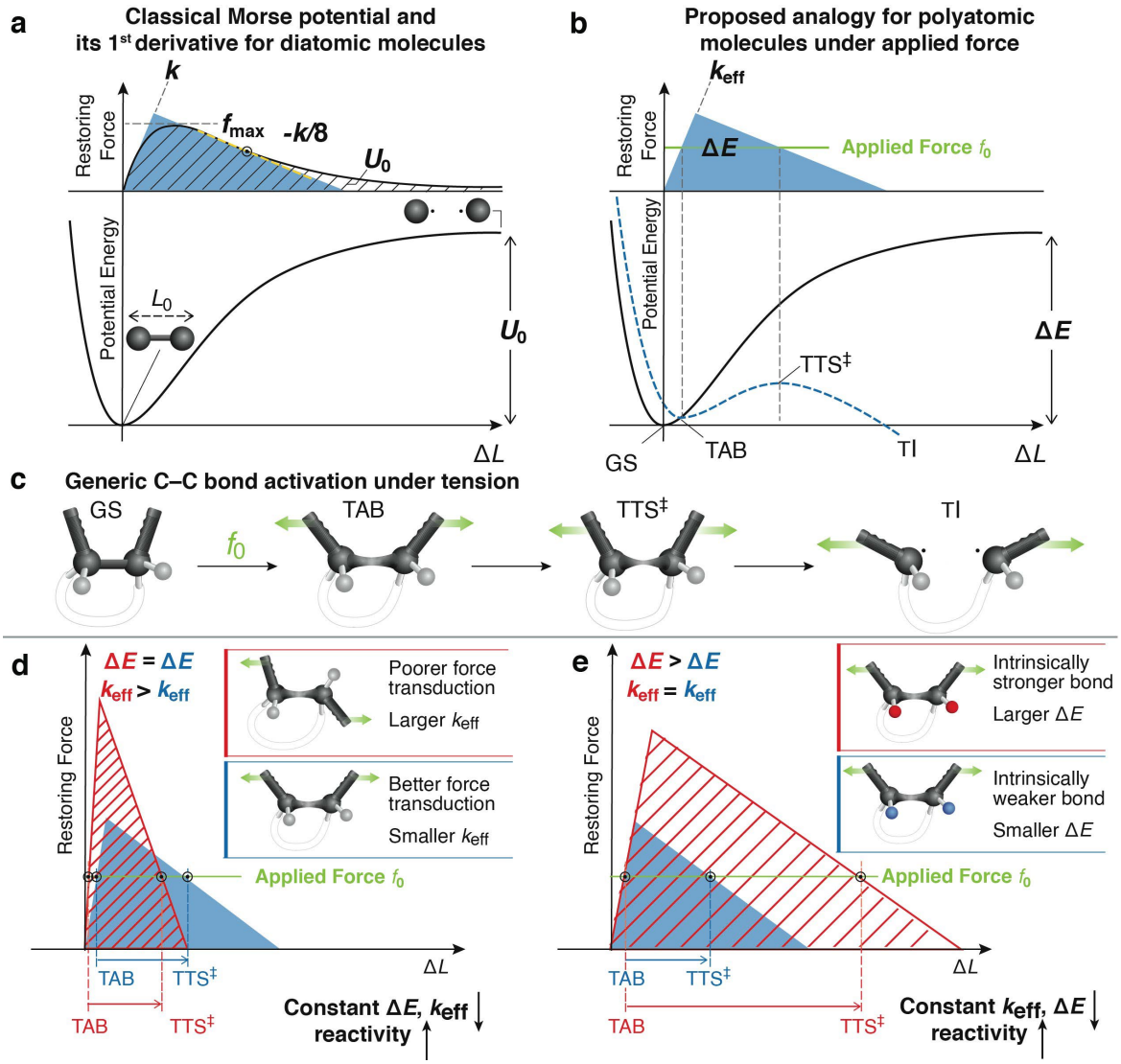

Fig. 1. **Schematic representation of the tension model of bond activation (TMBA).** (**a**) Illustration of the anharmonic Morse potential and its derivative for a diatomic molecule, depicting the relationship between the restoring force curve and the restoring force triangle. (**b**) Representation of the force-modified potential energy surface (FMPES) profile for a polyatomic molecule under static tension (f_0) and its correspondence with the restoring force triangle. (**c**) Schematic diagrams of the tension-activated bond (TAB), the tensioned transition state (TTS), and the tensioned intermediate (TI). (**d**) Influence of the effective force constant (k_{eff}) on the position of TAB, TTS, and the maximum force (f_{max}) for C–C bonds with identical energy change (ΔE) but varying k_{eff} values. (**e**) Influence of the energy change (ΔE) on the position of TAB, TTS, and f_{max} for C–C bonds with identical handle stereochemistry but different ΔE values resulting from electronic perturbations caused by the substituents.

We use the restoring force triangle to qualitatively understand C–C bond reactivity under tension. For C–C bonds that have identical ΔE (same area under the triangle) but distinct k_{eff} values (e.g.,

cis vs trans configuration) (**Fig. 1d**), the one that exhibits a smaller k_{eff} corresponds to a more deformed TAB and a lower f_{max}, implying higher reactivity under tension (**Fig.1d**). Conversely, for a pair of molecules with handles of identical stereochemistry but differing in substituents that exert electronic influences on the C–C bond and/or the developing radical character, ΔE is anticipated to differ while the k_{eff} values are nearly identical. In this scenario, the position of the TAB is unchanged, but the one with the smaller ΔE exhibits a lower f_{max} and an earlier TTS, indicating higher reactivity under f_0 (**Fig.1e**). Therefore, it is intuitive to expect that C–C bonds with lower resistance to deformation (i.e., smaller k_{eff}), or intrinsically more reactive (i.e., smaller ΔE) will display enhanced reactivity under tension. Based on these conjectures, we posit a physical organic model, termed the tension model of bond activation (TMBA), which captures the mechanochemical activation of C–C bonds in complex molecules using the two easily computed parameters: k_{eff} and ΔE.

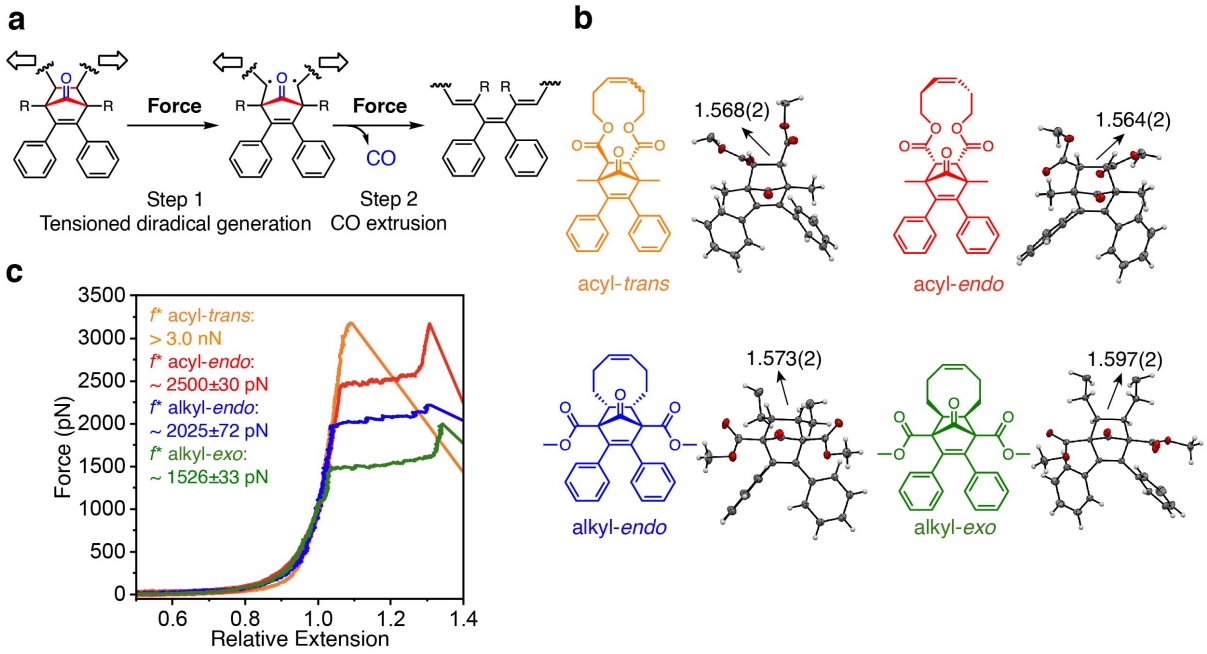

Fig. 2. NEO mechanophore moieties and the experimental characterizations. (**a**) Postulated stepwise mechanism of CO-releasing **NEO** mechanophores. (**b**) Chemical structures and corresponding single crystals of the four **NEO** derivatives. The lengths (Å) of the C–C bond cleaved in the diradical generation step are indicated, with the standard deviation in parentheses. The cycloalkene fragments are omitted for clarity. (**c**) Representative single-molecule force curves of **NEO** copolymers obtained through SMFS.

We developed the TMBA from mechanistic studies on the norborn-2-en-7-one (**NEO**) mechanophores[18]. In our initial report of **NEO** mechanochemistry[18], we proposed a unique stepwise activation mechanism involving two elementary steps, both of which include C–C bond cleavages (**Fig. 2a**). The widely used computational tool CoGEF (constrained geometries simulate external force)[19,20], however, failed to capture its critical aspects of the observed reactivity (fig. S3). We, therefore, initiated computational evaluations of isotensional activation energies using a rigorous method leading to insights that began to frame the TMBA. We also synthesized two new

NEO derivatives (**alkyl-*endo*** and **alkyl-*exo***) with the previously reported **acyl-*endo*** and **acyl-*trans*** to generate a set of structures with diverse stereochemistry and substituents (**Fig. 2b**) that impact k_{eff} and ΔE similarly to the examples illustrated in **Fig.1d** and **1e**. The physical organic insights gained from these mechanistic studies enabled us to refine and expand the qualitative TMBA into a parametric equation with broad applicability to predict mechanochemical C–C bond activation processes in numerous other mechanophores.

Distinct mechanochemical reactivities of four NEO derivatives

The four **NEO** derivatives depicted in **Fig. 2b** demonstrate variations in both functional groups and stereochemistry of the handles. These differences allow us to explore the influence of steric, electronic, and conformational factors on the stability of both the ground state and intermediate. The four **NEO** derivatives were incorporated in polymers and displayed distinct mechanochemical reactivities, as evidenced by ultrasonication and single-molecule force spectroscopy (SMFS) studies using an atomic force microscope[21]. In the ultrasonication experiments, all four derivatives exhibited mechanochemical activity when subjected to a pulsed acoustic field[1,4]. Competition studies ranked their relative mechanochemical reactivities as follows: *cis* > *trans*; *exo* > *endo*; alkyl > acyl (fig. S12). The SMFS analysis provided quantitative data on the transition force (f^*) required for activation[22-24] (**Fig. 2c**). Interestingly, the force-extension curve for the **acyl-*trans*** did not show a plateau prior to detachment, indicating an f^* beyond the measurable range (> 3.0 nN). In contrast, all three *cis* derivatives displayed distinct plateau regions, each characterized by different f^* values. Specifically, the f^* values were approximately 2500 ± 30, 2025 ± 72, and 1526 ± 33 pN for the respective *cis* derivatives (**Fig. 2c**). The trends observed in SMFS are consistent with the mechanochemical reactivity observed in the ultrasonication experiments. The significant impact of subtle structural variations on f^* prompted an extensive computational investigation to gain a deeper understanding of the relationship between structure and reactivity within the framework of the TMBA.

Mechanistic investigation of NEO activation

The external force explicitly included (EFEI) method[26,27] enabled us to locate the TAB, TTS, and TI on the FMPES. We thus computed the isotensional activation energies, $\Delta E^{\ddagger}$s, for each **NEO** derivative from low (0.25 nN) to high (5.25 nN) external force values. The EFEI method successfully identified barriers associated with the TTSs for both steps of the proposed two-step sequence in **Fig. 2a**. As noted previously and seen in the TMBA framework, the force required to lower $\Delta E^{\ddagger}$ to zero corresponds to f_{max} [28]. When the applied force is less than f_{max}, thermal energy becomes necessary in addition to the force to overcome the nonzero $\Delta E^{\ddagger}$ barrier. Since the EFEI calculations determine $\Delta E^{\ddagger}$ at each f_0 value, the reaction kinetics at a specific f_0 and temperature can be predicted using transition state theory.

To examine the accuracy of EFEI simulations for **NEOs**, we compared the predicted f^* with experimental SMFS studies. The f^* in SMFS reflects the force at which the chain extension rate is comparable to that of the mechanochemical reaction, which typically involves reaction half-lives of ~0.1 s [15, 25]. The corresponding $\Delta E^{\ddagger}$ for each mechanophore is ~16.0 kcal mol^{-1} at 298 K (**fig. S41**), as represented by the gray line in **Figs. 3a** and **3b**. Therefore, the calculated values of f^* were obtained from the points of intersection between the horizontal line and $\Delta E^{\ddagger}$. The predicted values

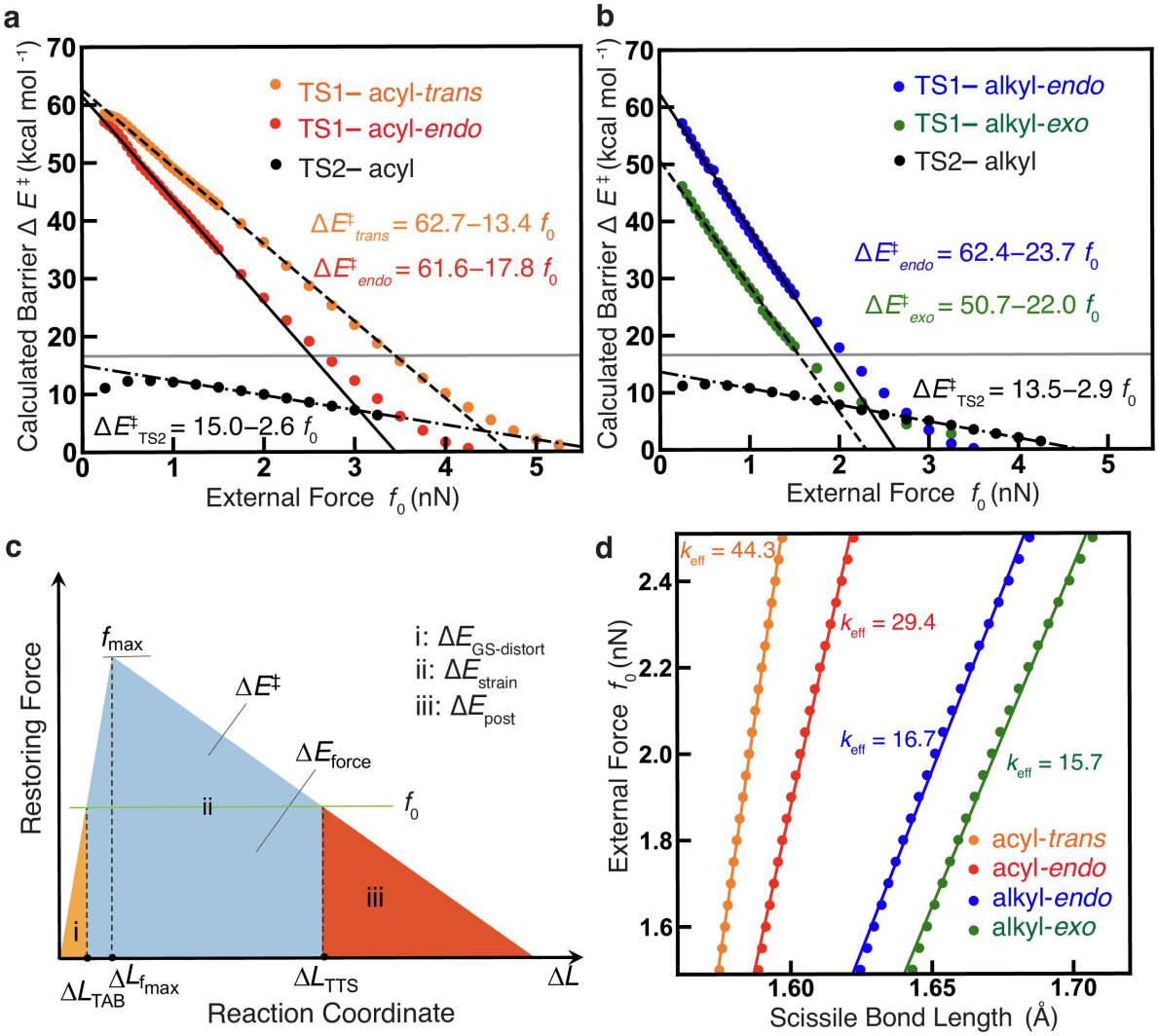

Fig. 3. **Electronic structure simulations on NEO derivatives and their connection to TMBA**. Panels (**a**) and (**b**) depict the EFEI-calculated activation energies for the four **NEO** mechanophores plotted against the applied force (f_0). The black dots represent the $\Delta E^{\ddagger}$ corresponding to the CO extrusion step from the respective diradical intermediates. The horizontal grey lines indicate the threshold of $\Delta E^{\ddagger}$, below which rapid thermal activation is expected based on transition state theory at 298 K and the timescale of SMFS experiment. Panel (**c**) utilizes the restoring force triangle to illustrate different segments of the reaction coordinate and the corresponding changes in electronic energy. The energy required for ground state distortion (orange, segment i) and post-transition state region (red, segment iii) is obtained through external mechanical force. The energy for the progression from TAB to TTS (blue, segment ii) is a combination of external mechanical work (ΔE_{force}) and external thermal energy ($\Delta E^{\ddagger}$). Panel (**d**) presents the computational data used to determine the effective stiffness (k_{eff}) for the four **NEO** mechanophores. The k_{eff} value quantifies the resistance of the bond to stretching when tension is applied remotely and transmitted through the handles to the scissile bond. The observed linear relationships provide support for the Hookean approximation of mechanophores in the vicinity of the GS.

of f^* are approximately 3.4, 2.6, 2.0, and 1.6 nN for **acyl-*trans***, **acyl-*endo***, **alkyl-*endo***, and **alkyl-*exo*** correspondingly, indicating a good agreement between simulation and experiments.

Qualitative mechanistic insight was gained from the force dependence of $\Delta E^{\ddagger}$s shown in **Figs. 3a** and **3b**. The $\Delta E^{\ddagger}$ of the initial C–C bond scission exhibits a monotonic decrease as f_0 increases. In contrast, the energy landscape for the CO-releasing step (indicated by black dots) appears relatively flat, particularly in the low-force region. The EFEI computed values of $\Delta E^{\ddagger}$ for the CO-releasing step are below the thermal threshold (grey line) for all values of f_0. This implies that the CO-releasing step proceeds spontaneously and rapidly during SMFS once the diradical intermediate is formed. In contrast, the $\Delta E^{\ddagger}$ for the initial C–C bond scission is significantly higher than the thermal threshold in the low force region but rapidly approaches the threshold with increasing f_0. Furthermore, while the $\Delta E^{\ddagger}$ of the first step experiences a more rapid change, it consistently remains higher than that of the CO-releasing step across the low force range (< 3 nN) for all **NEO** variants. This computational result suggests diradical generation as the RDS under typical experimental force conditions.

The plots presented in **Figs. 3a** and **3b** highlight quantitative aspects of the relationship between structure and reactivity of C–C bonds under tension. These plots exhibit a linear relationship in the low to intermediate force range (0.25-1.5 nN)[15]. The slope and intercept obtained from linear regression analysis hold significant implications in the context of the TMBA. First, the force-free activation energy ($\Delta E^{\ddagger}|_{f=0}$) represents the inherent reactivity of the mechanophore. **Figures. 3a** and **3b** show that the *trans* derivative and the two *endo* derivatives have similar $\Delta E^{\ddagger}|_{f=0}$ values of approximately 62 kcal•mol^{-1} for the first C–C bond scission. In contrast, the *exo* isomer exhibits a significantly lower $\Delta E^{\ddagger}|_{f=0}$ value of approximately 51 kcal•mol^{-1}. This lower $\Delta E^{\ddagger}|_{f=0}$ value indicates an enhanced inherent reactivity of the **alkyl-*exo*** compared to the other derivatives. Indeed, an elongated C–C bond in the alkyl-*exo* derivative is observed in single crystal structures (**Fig. 2b**). The slopes of the linear regressions reveal the sensitivity of the mechanophore's reactivity to applied tension and correspond to the mechanochemical coupling constant (γ)[15]. From **Figs. 3a** and **3b**, it can be observed that the *cis* configurations are more responsive to tension compared to the *trans* configuration, which is consistent with observations made for other mechanophores[24,28]. Therefore, the higher reactivity of the **acyl-*endo*** relative to the **acyl-*trans*** under tension is attributed to mechanochemical coupling effects rather than inherent reactivity differences. Also, the alkyl handles lead to enhanced mechanochemical coupling compared to acyl handles, resulting in the higher reactivity of the **alkyl-*endo*** relative to the **acyl-*endo***.

Development of the quantitative TMBA

Analyzing the EFEI calculations at various stages along the reaction pathway, including the transition from the force-free GS to the TAB, from the TAB to the TTS, and the post-TTS segment, provides insights into the influence of tension on energetic changes and tension-induced distortions and helps elucidate the molecular features that govern the observed differential reactivity among the **NEO** derivatives within the TMBA framework (fig. S23). When molecular distortions occur from the GS to ΔL_{TAB}, there is an associated increase in electronic energy, referred as $\Delta E_{GS\text{-}distort}$, represented by area i on the restoring force triangle (**Fig. 3c**). As the C–C bond extends from position ΔL_{TAB} to ΔL_{TTS}, the electronic energy further increases, as indicated by area ii. Finally, the electronic energy change accompanying the post-TTS region (ΔE_{post}) of the reaction coordinate

is represented by area iii. The total area enclosed within the restoring force triangle, ΔE, encompasses the sum of all electronic energies represented by areas i, ii, and iii. In progressing from ΔL_{TAB} to ΔL_{TTS}, external mechanical work contributes energy (ΔE_{force}, bottom rectangular area) equivalent to $-f_0 \bullet (\Delta L_{TTS} - \Delta L_{TAB})$, effectively reducing the barrier height to $\Delta E^{\ddagger} = ii + \Delta E_{force}$ (where ΔE_{force} is a negative value). Thermal energy ($\Delta E^{\ddagger}$, top triangular area) assists to overcome this barrier[17]. Thus, under tension, mechanical work fully contributes the energies associated with the initial and final distortions along the reaction coordinate, specifically areas i and iii. Area ii is supplied by a combination of mechanical work and thermal energy. As visualized by the restoring force triangle, as f_0 increases, the positions of ΔL_{TTS} and ΔL_{TAB} move closer together, ultimately converging at ΔL_{fmax} when f_0 reaches f_{max}. As a result, area ii decreases from a value of ΔE at f_0=0 to a value of zero at f_0=f_{max}.

Next, we utilized this segmentation to analyze the EFEI calculations of the four **NEO** derivatives. Drawing inspiration from the activation strain model, which has proven successful in elucidating the reactivity of various thermal reactions[30,31], we defined ΔE_{strain} as the energy difference between positions ΔL_{TTS} and ΔL_{TAB}, as determined by the EFEI calculations. This energy change is visually represented as area ii in **Fig. 3c**. We investigated the EFEI calculated dependence of ΔE_{strain} and ΔE_{force} on f_0 within the range of 0.25 nN to 2.50 nN for the four **NEO** derivatives. In the force regions of 1.5–2.5 nN where experimental scission was observed, the four **NEO** variants exhibit distinct ΔE_{strain} values, differing by up to 30 kcal•mol^{-1} (fig. S24). Importantly, these ΔE_{strain} trends align with the experimental reactivities ranking the structural features according to ΔE_{strain} as follows: *exo* < *endo*; alkyl < acyl; *cis* < *trans*. In contrast, the variations in ΔE_{force} among the four **NEO** derivatives are less profound (fig. S24), and the ΔE_{force} values do not correlate with experimental reactivities.

In considering how the structural features influenced $\Delta E_{GS\text{-}distort}$ and ΔE_{post} (areas i and iii), we analyzed on the scissile C–C bond length in both the TAB and TTS structures as a function of f_0. Interestingly, the four **NEO** variants exhibit distinct distortions at ΔL_{TAB}, with the **alkyl-*exo*** derivative showing the greatest stretching, followed by the **alkyl-*endo*** and then the acyl derivatives. By comparison, the **acyl-*trans*** derivative exhibits the least distortion (fig. S24). The f_0 dependent distortions at ΔL_{TTS} are more similar among the NEO variants until approximately 2.0 nN. These results suggest that $\Delta E_{GS\text{-}distort}$ plays a more significant role than ΔE_{post} in influencing mechanochemical reactivity. Thus, we conclude that the distinct γ values of **NEOs** are mainly contributed by differing $\Delta E_{GS\text{-}distort}$ with some contributions from ΔE_{force}.

EFEI calculations employed in this study are computationally intensive and pose significant challenges, rendering them impractical for the iterative design and accelerated discovery of new mechanophores. We posit that the TMBA offers a framework for developing a more accessible yet still predictive parametric calculation of mechanophore reactivity. In practical terms, we sought to correlate k_{eff} and ΔE in the TMBA with the slope (γ) and intercept (force-free $\Delta E^{\ddagger}$) observed in the linear correlations shown in **Figs. 3a** and **3b**. We first reasoned that mechanophores can be treated as Hookean objects, responding to force with an extent of GS distortion described by k_{eff}. For instance, C–C bonds with higher resistance to deformation (larger k_{eff}) will exhibit a smaller $\Delta E_{GS\text{-}distort}$ for a given f_0, as conceptualized in **Fig. 1d**. The stiffness constant is hypothesized as an alternative for $\Delta E_{GS\text{-}distort}$ that reflects how deformation depends on force. Consistent with Hammond's postulate[32], ΔE for the formation of the diradical intermediate estimates the relative

extension in the transition state (as conceptualized in **Fig. 1e**). As ΔE_{force} is controlled by the displacement between TAB and TTS (ΔL_{TTS} - ΔL_{TAB}) at a certain f_0, we reason that ΔE correlates with ΔE_{force}. For instance, a late transition state (large $\Delta L_{TTS} - \Delta L_{TAB}$) is expected for C–C bonds that are intrinsically more stable (larger ΔE) and have more negative ΔE_{force}. Moreover, we envisioned that ΔE approximates the force-free $\Delta E^{\ddagger}$ based on the Bell-Evans-Polanyi principle [33]. Therefore, both the slope and the intercept in **Figs. 3a**,**3b** are envisioned to correlate with ΔE and k_{eff}, suggesting the possibility of directly predicting the force required to reach a certain $\Delta E^{\ddagger}$ with only these two parameters. We chose the prediction of f^* exhibited in SMFS studies as the target where the mechanophore reactivity corresponds to force-coupled activation barriers of ~ 16–17 kcal mol^{-1} [15,24,25].

To assess the Hookean spring-like behavior of the scissile C–C bond near the GS, a computational force was incrementally applied through the handles in 0.05 nN intervals within the range of 1.5-2.5 nN, and the molecules were optimized to the resulting TAB. A linear correlation between the f_0 and C–C bond length was observed for all four **NEO** variants. The slope provided the constant k_{eff}, which was determined to be 29.4, 44.3, 16.7, and 15.7 nN Å^{-1} for **acyl-*endo***, **acyl-*trans***, **alkyl-*endo***, and **alkyl-*exo***, respectively (**Fig. 3d**). This Hookean-like behavior was found to be a general feature for an additional 27 mechanophores with known f^* in SMFS, encompassing cyclopropane, cyclobutane, and cyclobutene moieties (figs. S32-34).

To predict the experimental f^* for C–C bond activation events, we computed the ΔE values for a total of 31 mechanophores. Using a multivariate linear regression model, we investigated the relationship between the $f^*$and the two key parameters k_{eff} and ΔE. Remarkably, we found that employing these two parameters for multivariate linear regression can predict f^* for 23 mechanophores with high accuracy including **NEO,** cyclopropane, and cyclobutane moieties. The resulting model demonstrated a mean absolute error (MAE) of 0.18 nN and an R^2 value of 0.87, indicating a strong correlation between the predicted and experimental f^* values (**Fig. 4a**). Several additional cross-validation tests confirmed the robustness of the model. However, we noted that this predictive model did not accurately capture the behavior of seven cyclobutene mechanophores (fig. S35). As these seven cyclobutenes may follow an electrocyclic ring-opening mechanism that evades the diradical intermediate, we performed a separate linear regression on the cyclobutene mechanophores showing improved accuracy (fig. S36). These findings suggest that while the coefficients in the TMBA may vary depending on the specific mechanophore activation mechanism, the general predictive framework based on k_{eff} and ΔE remains valid.

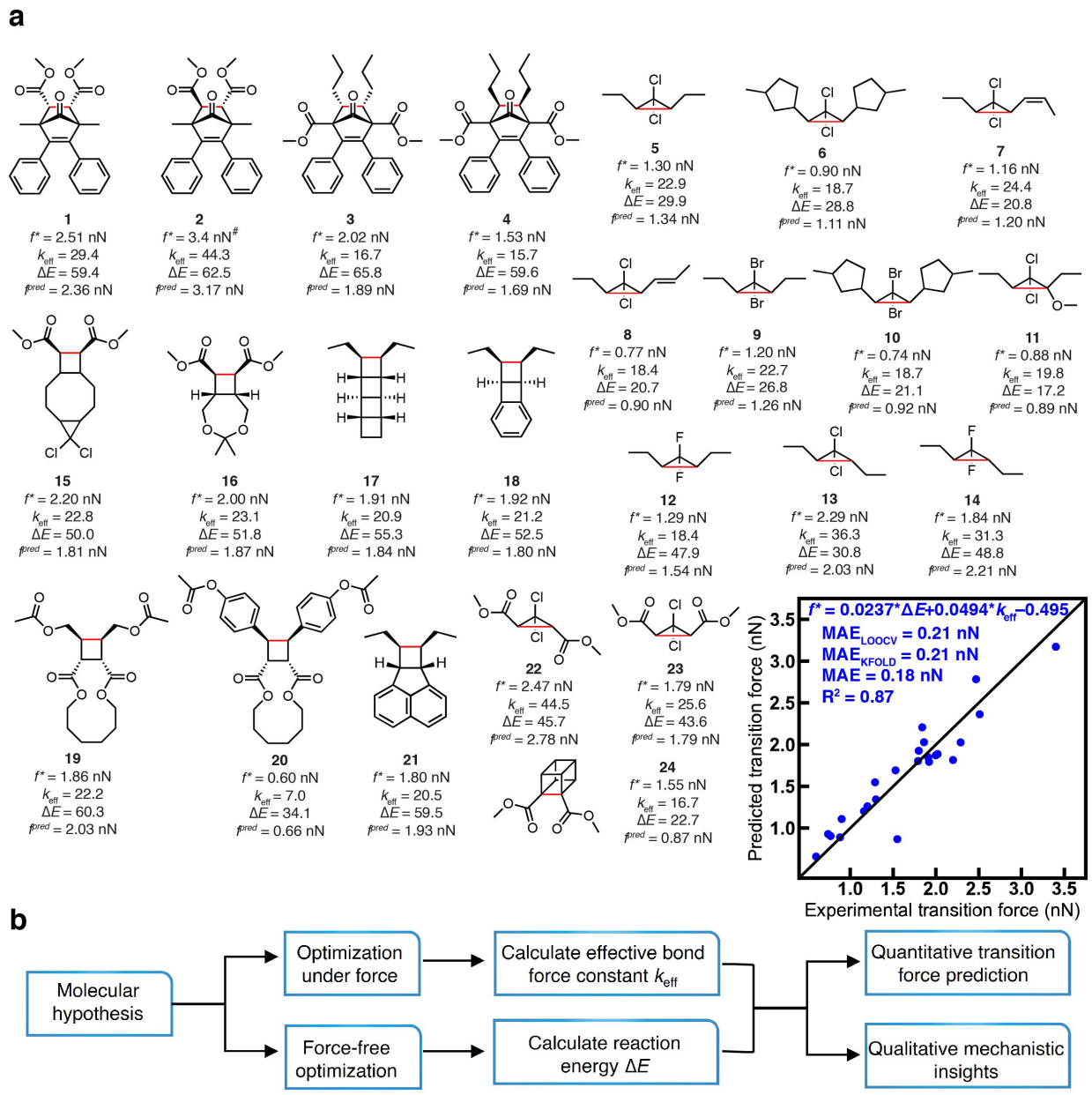

Fig. 4. **The linear model for predicting reactivity under force.** (**a**) Multivariate linear regression model for the prediction of experimental transition forces (f^*). The chemical structures depict the experimental f^* and calculated parameters used in the trained model. MAE_{LOOCV} represents the mean absolute error obtained from leave-one-out cross-validation (LOOCV), where each mechanophore serves as the test set while the remaining mechanophores are used for multivariate regression. MAE_{KFOLD} refers to the average MAE from repeated k-fold cross-validation with 80:20 train/test splits and 100 randomized splits. #Note that for **acyl-*trans***, the simulated f^* from EFEI calculations was utilized due to the absence of experimental SMFS data. (**b**) Workflow illustrating the application of the model to mechanophores in this work and potentially other mechanophores.

The TMBA approach offers several advantages, including its computational efficiency compared to CoGEF or EFEI simulations. Additionally, it provides immediate insights into structure-reactivity trends, where lower k_{eff} values indicate improved mechanochemical coupling and lower ΔE values suggest more favorable intrinsic reactivity. For example, mechanophores **6** and **10** have identical k_{eff} values but different ΔE values, indicating that the lower f^* of mechanophore **10** is primarily influenced by thermodynamic effects (**Fig. 4a**). Similarly, mechanophore **6** exhibits similar ΔE but a smaller k_{eff} compared to mechanophore **5**, suggesting enhanced mechanochemical coupling due to the presence of cyclopentenyl handles, consistent with previous studies[5]. Moreover, replacing alkyl handles with aryl handles in mechanophore **19** results in improved coupling and more favorable intrinsic activation, leading to a significant decrease in the f^* observed in **20**[34]. A straightforward computational workflow is depicted in **Fig. 4b**.

Conclusions

While the Morse potential has been utilized as the very first mechanochemistry model[16,35] and the restoring force plot has been proposed to understand bond activation upon stretching[17,36], the current work identifies two key molecular features (i.e., k_{eff} and ΔE) that captures the behaviors of bonds under external force from these known models. We then took advantage of the unique **NEO** platform, where a wide range of mechanochemical reactivities were accessed using a series of derivatives with high structural homology, to further extend the qualitative analysis to the quantitative prediction of the C–C bond mechanochemical activation process.

From our results, the complex kinetic behavior of tensioned bonds can be reduced to two simple parameters across various C–C activation mechanophores that have distinct core structures. We note that while the f^* in SMFS was chosen in this work to fairly compare different mechanophores with experimental data, the multivariate linear regression in TMBA presumably applies to any force values that correspond to other kinetic regions. We envision that the TMBA can be generalized to other mechanochemical bond scission processes beyond C–C activation. Specifically, qualitative physical organic insights can be obtained by simply calculating k_{eff} and ΔE values for computational screening of new mechanophores. Quantitative f^* value prediction can be performed by establishing the linear regression when having a series of experimental data or comprehensive electronic simulation results (e.g., EFEI) available. The simplicity and accessibility of TMBA will facilitate the discovery of new mechanophores and enhance our understanding of structure-reactivity relationships, leading to advancements in the field of mechanochemistry.

References:

1. Li, J., Nagamani, C. & Moore, J. S. Polymer mechanochemistry: from destructive to productive. *Acc. Chem. Res*. **48**, 2181–2190 (2015).
2. Lenhardt, J. M. et al. Trapping a diradical transition state by mechanochemical polymer extension. *Science* **329,** 1057–1560 (2010).
3. Hickenboth, C. R. et al. Biasing reaction pathways with mechanical force. *Nature* **446**, 423–427 (2007).
4. Caruso, M. M. et al. Mechanically-induced chemical changes in polymeric materials. *Chem. Rev*. **109,** 5755–5798 (2009).
5. Klukovich, H. M., Kouznetsova, T. B., Kean, Z. S., Lenhardt, J. M. & Craig, S. L. A backbone lever-arm effect enhances polymer mechanochemistry. *Nat. Chem*. **5,** 110–114 (2013).
6. Wang, J. et al. A remote stereochemical lever arm effect in polymer mechanochemistry. *J. Am. Chem. Soc*. **136**, 15162–15165 (2014).
7. Chen, Y., Mellot, G., Van Luijk, D., Creton, C. & Sijbesma, R. P. Mechanochemical tools for polymer materials. *Chem. Soc. Rev*. **50**, 4100–4140 (2021).
8. Liu, Y. et al. Flyby reaction trajectories: chemical dynamics under extrinsic force. *Science*. **373,** 208–212 (2021).
9. Nixon, R. & De Bo, G. Three concomitant C–C dissociation pathways during the mechanical activation of an N-heterocyclic carbene precursor. *Nat. Chem*. **12,** 826–831 (2020).
10. Chen, Y. et al. Mechanically induced chemiluminescence from polymers incorporating a 1,2-dioxetane unit in the main chain. *Nat. Chem*. **4**, 559–562 (2012).
11. Chen, Z. et al. Mechanochemical unzipping of insulating polyladderene to semiconducting polyacetylene. *Science* **357**, 475–479 (2017).
12. Wang, Z. et al. Toughening hydrogels through force-triggered chemical reactions that lengthen polymer strands. *Science* **374**, 193–196 (2021).
13. Wang, S. et al. Facile mechanochemical cycloreversion of polymer cross-linkers enhances tear resistance. *Science* **380**, 1248–1252 (2023).
14. Ribas-Arino, J. & Marx, D. Covalent mechanochemistry: theoretical concepts and computational tools with applications to molecular nanomechanics. *Chem. Rev*. **112**, 5412–5487 (2012).
15. Brown, C. L. et al. Substituent effects in mechanochemical allowed and forbidden cyclobutene ring-opening reactions. *J. Am. Chem. Soc*. **143**, 3846–3855 (2021).
16. Kauzman, W. & Eyring, HThe viscous flow of large molecules. *J. Am. Chem. Soc*. **62,** 3113 –3125 (1940).
17. Odell, J. A., Muller, A. J., Narh, K. A. & Keller, A. Degradation of polymer solutions in extensional flows. *Macromolecules*. **23**, 3092–3103 (1990).
18. Sun, Y. et al. Mechanically triggered carbon monoxide release with turn-on aggregation-induced emission. *J. Am. Chem. Soc*. **144**, 1125–1129 (2022).
19. Beyer, M. K. The mechanical strength of a covalent bond calculated by density functional theory. *J. Chem. Phys*. **112,** 7307–7312 (2000).
20. Klein, I. M., Husic, C. C., Kovács, D. P., Choquette, N. J. & Robb, M. J. Validation of the CoGEF method as a predictive tool for polymer mechanochemistry. *J. Am. Chem. Soc*. **142**, 16364–16381 (2020).

21. Binnig, G., Quate, C. F. & Gerber, C. Atomic force microscope. *Phys. Rev. Lett*. **56**, 930–993 (1986).
22. Zhang, Y. et al. Distal conformational locks on ferrocene mechanophores guide reaction pathways for increased mechanochemical reactivity. *Nat. Chem*. **13,** 56–62 (2021).
23. Horst, M. et al. Understanding the mechanochemistry of ladder-type Ccyclobutane mechanophores by single molecule force spectroscopy. *J. Am. Chem. Soc*. **143,** 12328–12334 (2021).
24. Wang, J. et al. Inducing and quantifying forbidden reactivity with single-molecule polymer mechanochemistry. *Nat. Chem*. **7**, 323–327 (2015).
25. Kbulatov, S. & Boulatov, R. Experimental polymer mechanochemistry and its interpretational frameworks. *ChemPhysChem.* **18,** 1422–1450 (2017).
26. Ong, M. T., Leiding, J., Tao, H., Virshup, A. M. & Martínez, T. J. First principles dynamics and minimum energy pathways for mechanochemical ring opening of cyclobutene. *J. Am. Chem. Soc*. **131,** 6377–6379 (2009).
27. Ribas-Arino, J., Shiga, M. & Marx, D. Understanding covalent mechanochemistry. *Angew. Chem. Int. Ed.* **48,** 4190–4193 (2009).
28. Ribas-Arino, J., Shiga, M. & Marx, D. Mechanochemical transduction of externally applied forces to mechanophores. *J. Am. Chem. Soc*. **132**, 10609–10614 (2010).
29. Kryger, M. J., Munaretto, A. M. & Moore, J. S. Structure–mechanochemical activity relationships for cyclobutane mechanophores. *J. Am. Chem. Soc*. **133,** 18992–18998 (2011).
30. Bickelhaupt, F. M. & Houk, K. N. Analyzing reaction rates with the distortion/interaction-activation strain model. *Angew. Chem. Int. Ed*. **56,** 10070–10086 (2017).
31. Bickelhaupt, F. M. Understanding reactivity with Kohn–Sham molecular orbital theory: E2–S$_N$2 mechanistic spectrum and other concepts. *J. Comput. Chem*. **20,** 114–128 (1999).
32. Hammond, G. S. A correlation of reaction rates. *J. Am. Chem. Soc*. **77**, 334–338 (1955).
33. Evans, M. G. & Polanyi, M. Inertia and driving force of chemical reactions. *Trans. Faraday Soc.* **34,** 11–24 (1938).
34. Wang, S. et al. Mechanism dictates mechanics: a molecular substituent effect in the macroscopic fracture of a covalent polymer network. *J. Am. Chem. Soc*. **143**, 5269–5276 (2021).
35. Crist, B., Oddershede, J., Sabin, J. R., Perram, J. W. & Ratner, M. A. Polymer fracture–a simple model for chain scission. *J. Polym. Sci. A: Polym. Phy.* **22**, 881–897 (1984).
36. De Boer, J. H. The influence of van der Waals' forces and primary bonds on binding energy, strength and orientation, with special reference to some Artificial resins. *Trans. Faraday Soc.* **32**, 10–37 (1936).

Acknowledgments: We thank Shu Wang for the discussion on Morse potential and its derivatives, and Dorothy Loudermilk for figure designs.

Funding: This work was supported by the NSF Center for the Chemistry of Molecularly Optimized Networks (MONET), CHE-2116298.

Author contributions:

Y.S., and I.K. contributed equally to this work. Y.S., I.K., and J.S.M. conceived the idea. Y.S. conducted the synthetic experiments and solution ultrasonication. Z.P.B. performed some of the monomer synthesis. I.K. conducted the DFT calculations and linear regression. T.B.K. conducted the single-molecule force spectroscopy measurement. S.L.C., H.J.K., and J.S.M supervised the project. Y.S. and I.K. wrote the original manuscript and all authors participated in the review and editing.

Competing interests: Authors declare that they have no competing interests.

Data and materials availability: Crystallographic data is available free of charge from the Cambridge Crystallographic Data Centre under reference CCDC nos. 2278660, 2278661. All other data are available in the main text or the supplementary materials.

Supplementary Materials

Materials and Methods

Supplementary Text

Figs. S1 to S68

Tables S1 to S10